

Colossal permittivity in high-entropy CaTiO_3 ceramics by chemical bonding engineering

Received: 26 January 2025

Accepted: 15 April 2025

Published online: 29 April 2025

Jinghan Cai¹, Shun Lan¹, Bin Wei^{1,2}, Junlei Qi¹, Ce-Wen Nan¹ & Yuan-Hua Lin¹✉

Dielectrics with high permittivity, low dielectric loss, and good temperature stability are crucial for electronic components to meet the ever-increasing application demands. However, challenges remain in further optimizing dielectric properties due to the correlation between these parameters. Here, we propose a chemical bonding engineering strategy in high-entropy CaTiO_3 ceramics and realize colossal permittivity with low loss and excellent stability. Our results reveal that the high-concentration oxygen vacancy (V_{O}^{\bullet})-related defects and the decreased activation energy of grain/grain boundary led to a colossal permittivity dielectric behavior, which should be ascribed to the weakened chemical bonding and the reduced formation energy of defects confirmed by our first-principles calculation. Consequently, in the high-entropy CaTiO_3 ceramic, a permittivity of 2.37×10^5 , low loss of 0.005, and good temperature stability ($\leq \pm 15\%$) in -50 – 250 °C are simultaneously achieved. This finding implies that chemical bonding engineering may be a promising strategy for designing colossal permittivity materials and provides a broad opportunity for the development of other defect-dependent functional materials.

Dielectrics have widespread applications in electronic fields as fundamental components of electrostatic capacitors^{1,2}. The developing trend of device miniaturization has put forward higher requirements for dielectrics with colossal permittivity ($>10^4$), low dielectric loss, and excellent temperature stability. However, these key factors are strongly correlated in dielectric materials. For example, in BaTiO_3 -based dielectrics, the strong polarization contributes to a high permittivity ($>10^4$) near the Curie temperature, yet a large loss and severe temperature dependence due to the ferroelectric phase transition³. Besides, $\text{CaCu}_3\text{Ti}_4\text{O}_{12}$ ceramics show a colossal permittivity (CP) while maintaining satisfying temperature stability owing to a frustrated phase transition, yet the high dielectric loss (>0.1) limits its broader application⁴. On the other hand, paraelectric SrTiO_3 (STO) ceramics possess low dielectric loss (<0.01) and are almost temperature-independent, but suffer from an inferior permittivity (~ 300)⁵. As such, simultaneously achieving colossal permittivity, low dielectric loss, and

temperature-stable performance in dielectrics has been a big challenge and a common objective in this field.

The dielectric properties have been recognized to be directly correlated with the polarization process, including interfacial polarization and dipole polarization^{6–8}, suggesting possible ways of regulating the overall performance of dielectrics. Accordingly, various efforts have been made over the years to develop preferable dielectric materials based on the principle of polarization improvement. On the one hand, CP can be achieved in $\text{ACu}_3\text{Ti}_4\text{O}_{12}$ ($A = \text{Ca}, \text{Bi}_{2/3}, \text{La}_{2/3}, \text{Y}_{2/3}$, etc.)- and NiO-based ceramics by constructing a core-shell structure consisting of semiconducting grains and insulating grain boundaries, which originates from the enhanced interfacial polarization. For example, by forming abundant subgrains and the consequent polarized interfaces, the $\text{Y}_{2/3}\text{Cu}_3\text{Ti}_4\text{O}_{12}$ ceramics can achieve a giant permittivity of 4.49×10^5 , but is accompanied by an unexpectedly high loss (0.51)⁹. On the other hand, significantly improved permittivity can

¹State Key Laboratory of New Ceramics and Fine Processing, School of Materials Science and Engineering, Tsinghua University, Beijing, PR China. ²Henan Key Laboratory of Materials on Deep-Earth Engineering, School of Materials Science and Engineering, Henan Polytechnic University, Jiaozuo, PR China.

✉ e-mail: linyh@tsinghua.edu.cn

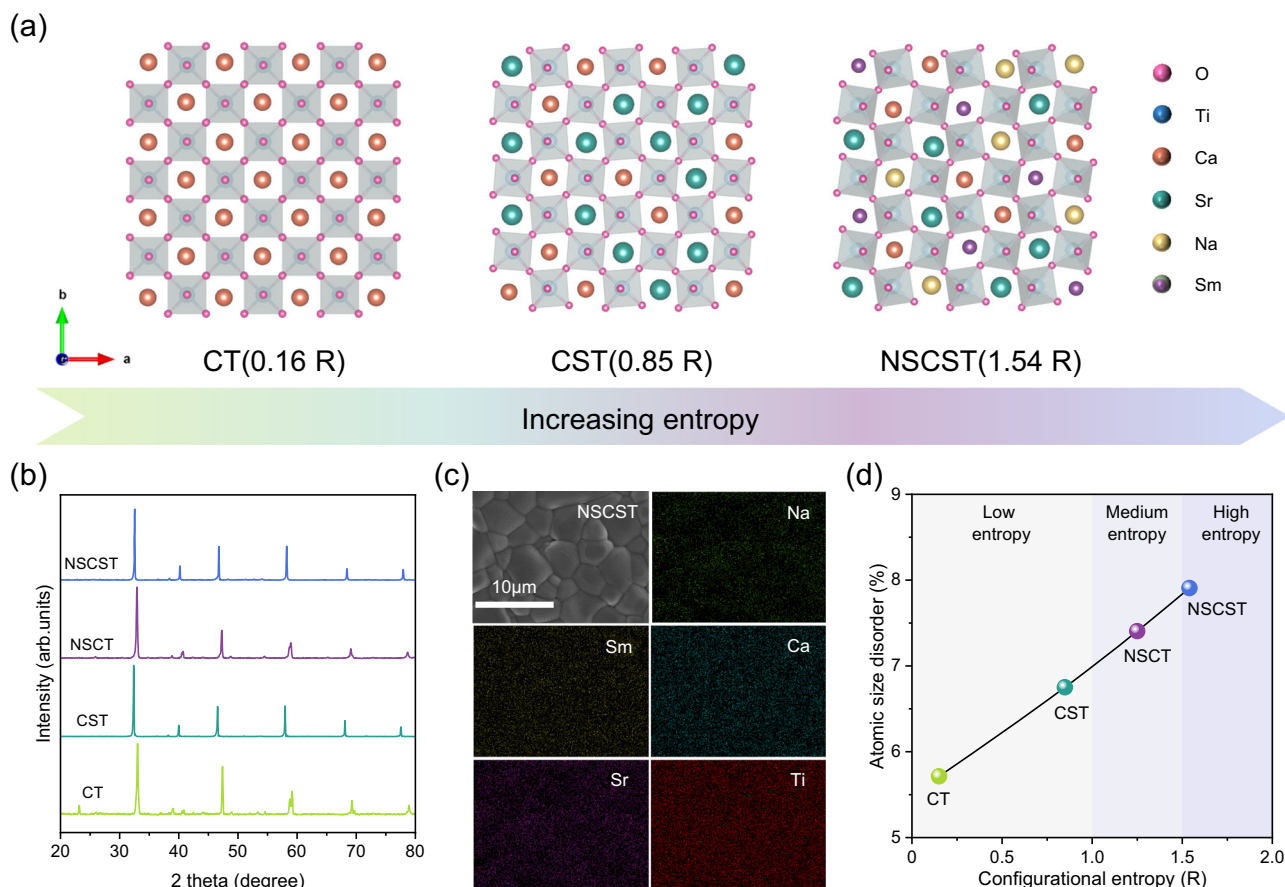


Fig. 1 | Evolution of phase and structure as a function of configurational entropy. **a** Schematic diagram depicting the progression of atomic disorder and lattice distortion as configurational entropy increases. **b** XRD patterns of the

entropy-regulated ceramics. **c** SEM images of the cross-sectional area with element mapping of the NSCST ceramic. **d** Atomic size disorder level as a function of configurational entropy.

also be realized in materials such as TiO_2 and STO ceramics. For instance, in Nb+In co-doped TiO_2 ceramics, CP ($\sim 6 \times 10^4$) and low dielectric loss (~ 0.05) can be obtained due to the defects induced by donor-acceptor co-doping⁸. In STO ceramic, CP ($\sim 2.8 \times 10^4$) and low dielectric loss (~ 0.007) can be realized due to the promoted production of $\text{V}_\text{O}^{\bullet}$ ¹⁰. However, a further increase in permittivity depends on high-concentration doping, leading to an inevitable increase in dielectric loss, which limits further performance improvements.

Recently, the high-entropy design strategy has been reported to be effective in achieving a higher concentration of defects in some high-entropy systems, e.g., $(\text{La}_{0.6}\text{Sr}_{0.4})(\text{Co}_{0.2}[\text{FeMnNiMg}]_{0.8})\text{O}_3$ ¹¹, which is mainly ascribed to the atomic disorder and lattice distortion^{12–14}. Inspired by these findings, we believe that this high-entropy approach is highly desirable for the design of CP materials, taking advantage of its probable defect-generating effects and expanded solid solubility. In this work, CaTiO_3 (CTO) was determined as the matrix material, considering its similar crystal structure to the reported defect-dependent CP ceramics. By the entropy design on its A-site, our results demonstrate a CP of 2.37×10^5 and an ultralow loss of 0.005 obtained in the high-entropy CTO ceramic. This high-entropy design approach is expected to provide a feasible method for the development of high-performance dielectrics.

Results and discussion

High-entropy design on CTO-based dielectric ceramics

Nb, Er co-doped CTO was determined to be the starting material based on previous experimental experience, and additional Sr, Na, and Sm were equimolarly incorporated into Ca sites. Ceramic samples with compositions of $\text{Ca}(\text{Ti}_{0.97}\text{Nb}_{0.015}\text{Er}_{0.015})\text{O}_3$ (CT), $(\text{Ca}_{0.5}\text{Sr}_{0.5})$

$(\text{Ti}_{0.97}\text{Nb}_{0.015}\text{Er}_{0.015})\text{O}_3$ (CST), $(\text{Na}_{0.33}\text{Sm}_{0.33}\text{Ca}_{0.33})(\text{Ti}_{0.97}\text{Nb}_{0.015}\text{Er}_{0.015})\text{O}_3$ (NSCT), and $(\text{Na}_{0.25}\text{Sm}_{0.25}\text{Ca}_{0.25}\text{Sr}_{0.25})(\text{Ti}_{0.97}\text{Nb}_{0.015}\text{Er}_{0.015})\text{O}_3$ (NSCST) were synthesized using the conventional solid-state reaction method (Table S1). The quantitative chemical compositions of the synthesized ceramics were confirmed by the XRF test results (Table S2). Figure 1a depicts the schematic diagram of the high-entropy design on the A-site of CT. Based on calculations and Rietveld refinements, the structures show an increasing atomic disorder and lattice distortion as more elements were introduced (Table S3).

The configurational entropy (S_config) is used to quantify the overall compositional inhomogeneity, defined as $S_\text{config} = -R[(\sum_{i=1}^N x_i \ln x_i)_{\text{cation-site}} + (\sum_{j=1}^M x_j \ln x_j)_{\text{anion-site}}]$, where R , $N(M)$, $x_i(x_j)$ represent the ideal gas constant, number of elements at the cation (anion) sites, and the molar ratio of the elements, respectively¹⁵. As more foreign elements randomly occupy equivalent A-site in CT, S_config gradually increases from 0.16 R (CT) to 1.54 R (NSCST), transitioning accordingly from low entropy ($S_\text{config} < 1$ R) through medium entropy ($1 \text{ R} \leq S_\text{config} < 1.5 \text{ R}$) to high entropy ($S_\text{config} \geq 1.5 \text{ R}$), and give rise to atomic size disorder ($\Delta\delta_\text{size}^*$) (Fig. 1d). The XRD results confirm that all samples possess a pure orthorhombic phase, and the slight peak position shift is consistent with the ionic size changes of the introduced A-site elements, verifying the sufficiency of the solid solution (Fig. 1b). EDS mapping of the NSCST sample shows a uniform and homogeneous dispersion of the constituent elements, demonstrating successful preparation of the high-entropy ceramic sample (Fig. 1c). Rietveld refinement of the XRD patterns further proves that all CTO-based ceramics have a pure $Pbnm$ structure. The merging or disappearance of some peaks or groups of peaks is the consequence of A-site compositional fluctuation, which affected lattice parameters and

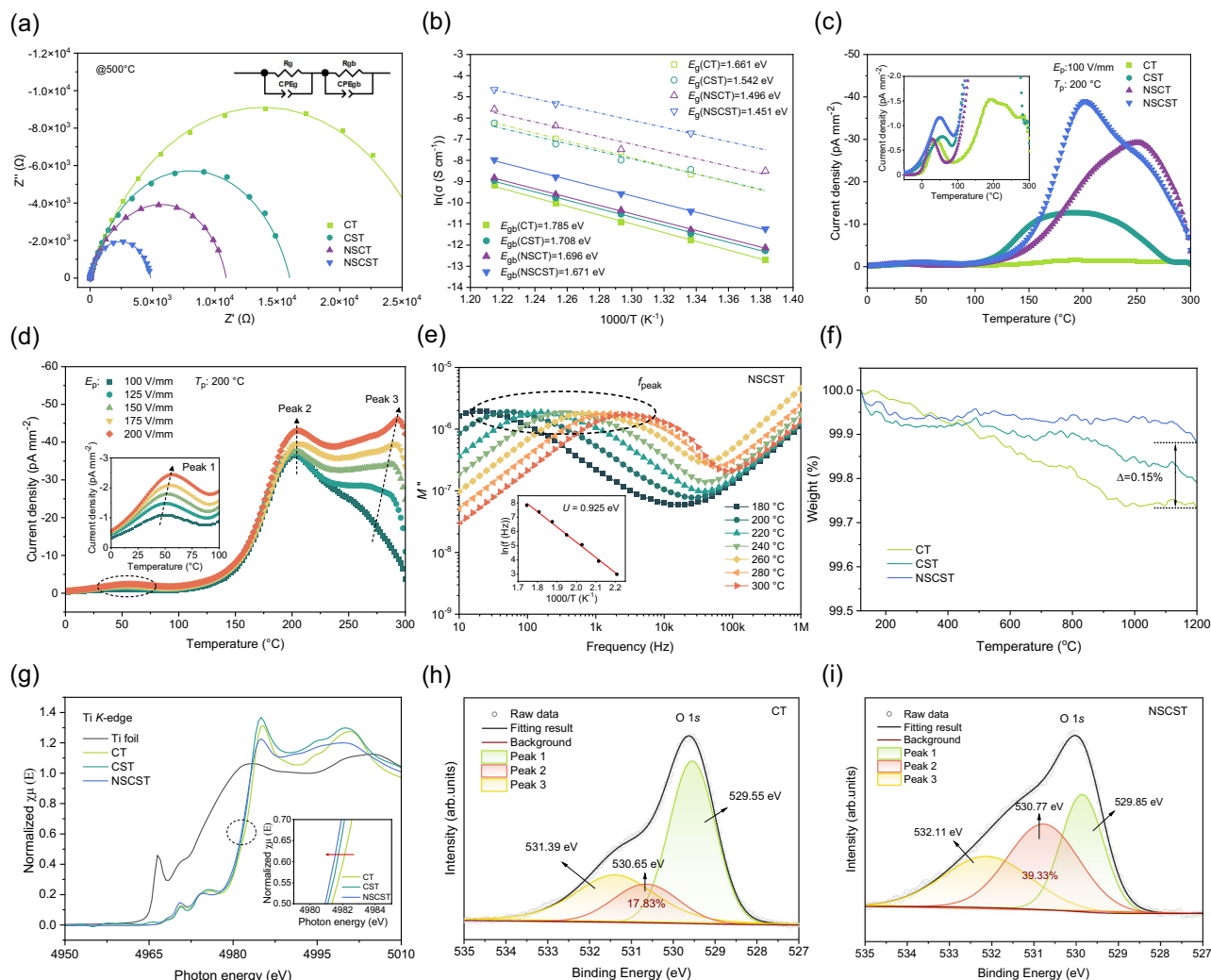


Fig. 2 | Electrical response and defect generation modified by the varying configurational entropy. **a** The complex impedance spectra of CTO-based ceramics measured at 500 °C. Inset: the equivalent circuit model, consisting of two sets of parallel combinations of a resistor and a constant phase element (CPE), representing grain (R_g , CPE_g) and grain boundary (R_{gb} , CPE_{gb}) response. **b** Fitting results of the grain (E_g) and grain boundary (E_{gb}) activation energies of CTO-based ceramics. **c** TSDC curves of CTO-based ceramics tested under a polarization voltage (E_p) of 100 V/mm and a polarization temperature (T_p) of 200 °C. Inset: detailed variation

in the low depolarization current density region. **d** TSDC curves of the NSCST ceramic ($T_p = 200$ °C, $E_p = 100$ –200 V/mm). Inset: magnified view of Peak 1. **e** The imaginary part of the electric modulus (M'') as a function of frequency for the NSCST ceramic. Inset: fitted activation energy (U) of the detected relaxation peaks circled by the dashed line. **f** TGA results of CT, CST, and NSCST, indicating the difference in weight loss degree (Δ) between CT and NSCST. **g** The Ti K-edge XANES spectra of CT, CST, and NSCST. Inset: enlarged view showing the absorption-edge position variation. **h, i** XPS O 1s spectra of CT (**h**) and NSCST (**i**).

diffraction patterns rather than phase transition^{16,17} (Figs. S1 and S2). Based on the refined lattice parameter data, the relative densities were calculated, revealing the compact structures obtained in all samples (Table S4), which is also supported by the cross-sectional SEM images (Fig. S3). The average grain size (AG) gradually increases as S_{config} increases. Based on compositional and electrical test results shown below, we propose that this facilitated grain growth in the high-entropy ceramics is due to the elevated concentration of oxygen vacancies, which promotes the mass transportation process during sintering^{18,19}. The above results together confirm the feasibility of applying the high-entropy strategy to construct CTO-based ceramics and provide more tunability for subsequent performance optimization.

Promoted defect generation by high-entropy design

To validate the feasibility of the high-entropy design in inducing more lattice defects, we conducted defect-related electrical measurements and valence state analysis. The complex impedance spectra of the CTO-based ceramics were measured at 500 °C and were fitted

according to the equivalent circuit^{20,21}, which reflects the electrical response from grains and grain boundaries, respectively (Fig. 2a). The spectra for all samples consist of one obvious arc attributed to the grain boundary response, while that of grains is indistinguishable due to their relatively small resistance. The arc diameter gradually decreased as more elements were introduced into the A-site of CTO, indicating a reducing trend of grain boundary resistance, which can be attributed to larger amounts of defects aggregated at the grain boundaries (Fig. S4). Meanwhile, the diameter of the arcs decreases with increasing temperature (Fig. S5), indicating a thermally activated process that follows the Arrhenius law: $\sigma_{gb} = \sigma_0 \exp(-E_{gb}/k_B T)$, where σ_{gb} is the grain boundary conductivity, σ_0 is the pre-exponential factor, E_{gb} is the activation energy of the grain boundary, and k_B is the Boltzmann constant. The experimental data were fitted accordingly (Fig. 2b), showing a decreasing trend of the activation energies as the entropy increases. Although the activation energy value varies slightly between samples, the grain boundary resistance is obviously minimal for NSCST, indicating the existence of a larger number of defects in the high-entropy ceramic. Moreover, the average value of the fitted grain

boundary activation energies for all samples is around 1.7 eV, higher than that of most STO-based CP systems^{10,22,23}, which is beneficial for the suppression of the dielectric loss.

Furthermore, TSDC tests were performed to determine the defect characteristics in entropy-regulated ceramics (Fig. 2c). Two groups of peaks can be seen in all four sets of data, where the one located at a higher temperature range shows an obvious increase in intensity as the entropy increases. To better understand the defect mechanism, TSDC curves of the NSCST ceramic tested under different polarization voltage (E_p) and temperature (T_p) were analyzed in detail (Fig. 2d). It has been reported that three types of defects, including trap charges, defect dipoles, and space charges (mainly referring to oxygen vacancies) can be distinguished from the positions at the TSDC relaxation curves^{24–26}. In our case, three peaks can be identified, distinguished by different peak temperatures (T_m) and denoted as Peak 1 ($50^\circ\text{C} < T_m < 55^\circ\text{C}$), Peak 2 ($205^\circ\text{C} < T_m < 210^\circ\text{C}$), and Peak 3 ($266^\circ\text{C} < T_m < 286^\circ\text{C}$), respectively (Fig. S6). Among these three peaks, Peak 1 and Peak 3 shift towards a higher temperature as E_p increases, which fits the characteristic of V_O^{\bullet} ²⁷. The position of Peak 2 remains still, and its maximum depolarization current density (J_m) increases linearly with E_p , corresponding to a defect dipole-related relaxation process^{26,28}. To further determine the exact defect types, an initial rise method²⁹ was used to calculate the activation energies: $\ln[J_D(T)] \cong \text{const.} - (E_a/k_B T)$, where J_D is the depolarization current density. Three activation energy values were calculated to be 0.238–0.242 eV (Peak 1), 0.578–0.715 eV (Peak 2), and 1.264–1.513 eV (Peak 3), corresponding to in-grain V_O^{\bullet} , defect dipoles, and across-grain-boundary V_O^{\bullet} respectively^{30–32} (Fig. S7). Considering the valence variability and relative content of the involved elements, V_O^{\bullet} and $\text{Ti}_{\text{Ti}}^{\prime}$ should be the dominant lattice defects, which can be shown as: $\text{Ti}_{\text{Ti}}^{\times} + e' \rightarrow \text{Ti}_{\text{Ti}}^{\prime}$, $\text{O}_O^{\times} \rightarrow V_O^{\bullet} + 2e' + \frac{1}{2}\text{O}_2 \uparrow$. Therefore, $\text{Ti}_{\text{Ti}}^{\prime}-V_O^{\bullet}-\text{Ti}_{\text{Ti}}^{\prime}$ would be the most likely existing form of the defect dipoles developed during sintering, which is supported by the similar activation energy value reported in the previous work³⁰. According to the mathematical definition of the dipole polarization intensity (P_e), the dipole concentration (N_d) can be evaluated by integrating the area under the corresponding peak²⁴. Results show a larger Peak 2 area for NSCST (Fig. S8), pointing to the highest dipole concentration in the high-entropy ceramic, consistent with the above discussions.

Generally, the defect characteristics can also be analyzed through relaxation behaviors that appear in the dielectric property-frequency diagram^{33,34}. The imaginary part of the electrical modulus M'' is used here to magnify potential defect signals of the NSCST ceramic in the finite frequency test range (Fig. 2e). M'' was calculated as follows: $M'' = \varepsilon'' / (\varepsilon'^2 + \varepsilon''^2)$, where ε' and ε'' are the real and imaginary parts of the complex relative permittivity. A group of relaxation peaks appears in the frequency range of $10\text{--}10^3$ Hz and shifts towards a higher frequency with increasing temperature, suggesting a faster polarization process³⁵: $f_{\text{peak}} = f_0 \exp(-U/k_B T)$, where f_{peak} is the peak frequency and f_0 is a constant. U was calculated to be 0.925 eV, suggesting the existence of oxygen vacancies at the grain boundaries, as confirmed by other reported experimental results of similar material systems^{35–38}. TGA test results can further verify the existence of oxygen vacancies (Fig. 2f). The evaporation effect of the physically adsorbed H_2O has already been excluded. The CT ceramics presented a drastic weight loss with the increase of temperature, while that of the NSCST ceramics is relatively gentle, indicating that a larger amount of oxygen vacancies exists in NSCST ceramics and mitigates the weight loss due to the compensating effect of the backfilled oxygen atoms^{39,40}. The Ti K -edge XANES spectra were collected to validate the generation of $\text{Ti}_{\text{Ti}}^{\prime}$ (Fig. 2g). The edge position showed a shift towards lower photon energy as the entropy increases, demonstrating a reduced average Ti valence and more $\text{Ti}_{\text{Ti}}^{\prime}$ in the high-entropy NSCST ceramics.

To directly visualize the variation of oxygen vacancy concentration after entropy regulation, XPS tests were conducted focusing on O

1s valence state changes (Fig. 2h, i, Fig. S9). Three peaks with binding energies of around 532 eV, 530.8 eV, and 529.7 eV were observed, attributed to the response of absorbed H_2O , oxygen vacancies, and lattice oxygen, respectively^{8,41,42}. The spectra vary obviously between samples, and the main difference comes from the intensity change of Peak 2, corresponding to the oxygen vacancy concentration. Compared to CT, Peak 2 shows a prominent enhancement in NSCST, indicating a promoted production of oxygen vacancies after entropy regulation. From the results and analysis above, it is proven that the high-entropy strategy is an effective approach for stimulating the production of defects, as expected.

To gain further insight into the nature of this high-entropy-induced defect generation, DFT calculations were performed on regulated CT supercells to visualize the structural evolution as a function of configurational entropy. Multiple O atoms were removed from the CT, CST, and NSCST ceramics to obtain structural information considering various defect quantities. Electron localization function (ELF) mappings from different views of CT, CST, and NSCST were simulated (Fig. 3a–d, Fig. S10 and S11), which reflect the localization extent of the reference electron. The ELF value ranges from 0 to 1, where 0 represents no electrons, and 1 corresponds to perfect localization⁴³. Along [512], local atom size disorder resulted in a certain degree of lattice distortion in NSCST (Fig. 3a, c). With Na, Sm, and Sr elements entering A-sites in CT, regions around O atoms appear to be darker, demonstrating a notably reduced covalency of the A/B–O bonds⁴⁴ as a result of the entropy modulation. These changes in the electron distribution are attributed to the diversity between different A-site atoms, which leads to changes in chemical bonding characteristics within the lattice. Further analysis focusing on unit bond strengths in entropy-regulated systems helps to quantify these bonding property differences with distinct intensity variations (Fig. 3e, f). The A–O bond shows a monotonically weakening bond strength as the entropy increases, regardless of the retracted amount of O atoms. Meanwhile, the high-entropy NSCST ceramic also presents the weakest B–O bond under equivalent circumstances, providing beneficial conditions for the A/B–O bond dissociation and the escape of O atoms⁴⁵. In addition, the defect formation energy (ΔE_{defect}) was calculated correspondingly as a descriptor for defect formation difficulty (Fig. 3g). Horizontally viewing, it would cost less energy to generate lattice defects in the high-entropy NSCST system. ELF simulations, each with 6 absent O atoms, were taken as comparative examples (Fig. 3b, d), visualizing lattice distortions and Ti–O bonding changes from the direction of [001]. Since the defect formation energy for CT exceeds zero, this structure with more absent O atoms can only stably exist in high-entropy NSCST ceramics. In other words, the weakened chemical bonding of NSCST ceramics is conducive to generating larger amounts of lattice defects, which explains our previous defect-related experimental results. The dipole moment (Δp) was also evaluated as a quantitative indicator pointing to overall dielectric performance (Fig. 3h). The NSCST ceramics exhibit a maximum dipole moment value, which is directly associated with enhanced polarization, validating the effectiveness of this high-entropy strategy. Additional DFT calculations are shown in Figs. S12 and S13, demonstrating a lower ICOBI value, a narrowed band gap, and a reduced effective mass of charge carriers with the increase of entropy, pointing to a more semiconductive characteristic in the high-entropy NSCST ceramic, which is in agreement with the tested activation energies and other experimental results.

Significantly improved dielectric performance in the high-entropy NSCST ceramics

Dielectric performance from all aspects was evaluated to further confirm the feasibility of achieving CP through the high-entropy strategy. The frequency dependence of dielectric properties, including permittivity and dielectric loss ($\tan\delta$), was measured at room

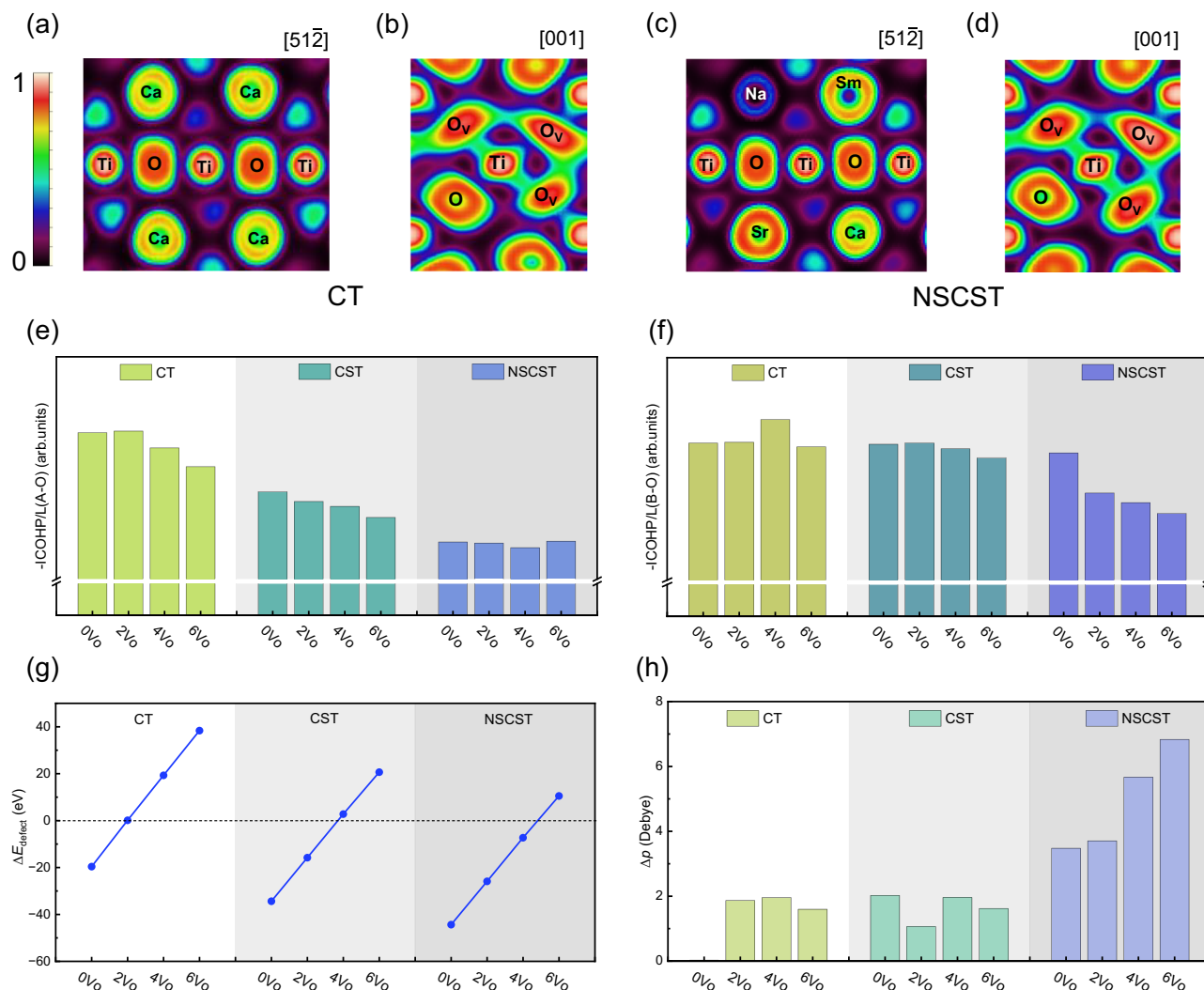


Fig. 3 | Simulations of local structure and defect formation evolutions with increasing entropy. **a–d** ELF mappings of CT (**a**, **b**) and NSCST (**c**, **d**) along different directions. **e**, **f** The integrated crystal orbital Hamilton populations (ICOHP) value in a unit bond length (L) of A–O (**e**) and B–O (**f**) for CT, CST, and NSCST

ceramics, indicating the bond strength changes as the entropy increased.

g, **h** Comparison of defect formation energy (ΔE_{defect}) (**g**) and the electric dipole moment ($\Delta\mu$) (**h**) between CT, CST, and NSCST ceramics.

temperature (RT) for CTO-based ceramics (Fig. 4a). All samples show frequency-independent characteristics in the low-frequency range, and undergo a slight degradation beyond 100 kHz. No obvious interfacial relaxation behaviors were detected in the low-frequency range, excluding major contributions from interface polarizations⁷. The permittivity also remained stable when applied with various DC bias voltages, confirming no electrode effect was involved in the achieved CP performance^{46,47} (Fig. S14). Specifically, in the low-entropy CT ceramic, both colossal permittivity (7.02×10^4) and low $\tan\delta$ (0.019) were obtained simultaneously, demonstrating that CP can also be achieved in the CTO matrix. As more substitutional elements were introduced into the A-site, the permittivity monotonically increased and reached an exceptional level of 2.37×10^5 in the high-entropy NSCST ceramic, while effectively maintaining an ultralow $\tan\delta$ of 0.005 (Fig. 4a, e). This remarkable evolution trend of permittivity reveals a close association between dielectric properties and configurational entropy and confirms the effectiveness of this strategy in achieving permittivity improvement. Thermal stability is also evaluated for CTO-based ceramics (Figs. 4b, S15). Each of them shows a good temperature-stable capacitance in the test temperature range (–50 to 250 °C). The detected loss increase at higher temperatures should be attributed to the migration of thermally activated carriers⁴⁸. Notably, the calculated

temperature coefficient ($\Delta C/C_{25^\circ\text{C}}$) value at 1 kHz for the high-entropy NSCST is within $\pm 15\%$ (Fig. 4c), sufficient to satisfy the temperature stability requirements of X9R capacitors ($\Delta C/C_{25^\circ\text{C}} \leq \pm 15\%$, –50 to 200 °C).

The intrinsic correlation between configurational entropy and dielectric performance needs to be further discussed and concluded. As a directly affected parameter of compositional change, the bond strengths of A–O and B–O show a distinct entropy-dependent performance (Fig. 4d). The enhancement of entropy leads to an increase in atomic size disorder and the change in electron distribution within the lattice⁴⁹. These effects are manifested as weakened bonding in the high-entropy NSCST, benefiting the bond dissociation process and the escape of oxygen atoms. The semiquantitative concentrations of oxygen vacancies in CT, CST, and NSCST were estimated based on XPS fitting results (Fig. 4d). Considering the requirements of charge conservation, corresponding amounts of electronegative defects would be generated for compensation, most likely Ti^{3+} in these titanium-based systems⁵⁰. With efficiently produced defects, including V_O and Ti^{3+} , the dipole polarization of CTO-based ceramics was significantly enhanced, eventually obtaining an exceptional dielectric performance in the high-entropy NSCST (Fig. 4e). A colossal permittivity of 2.37×10^5 , an ultralow $\tan\delta$ of 0.005, and a favorable frequency/

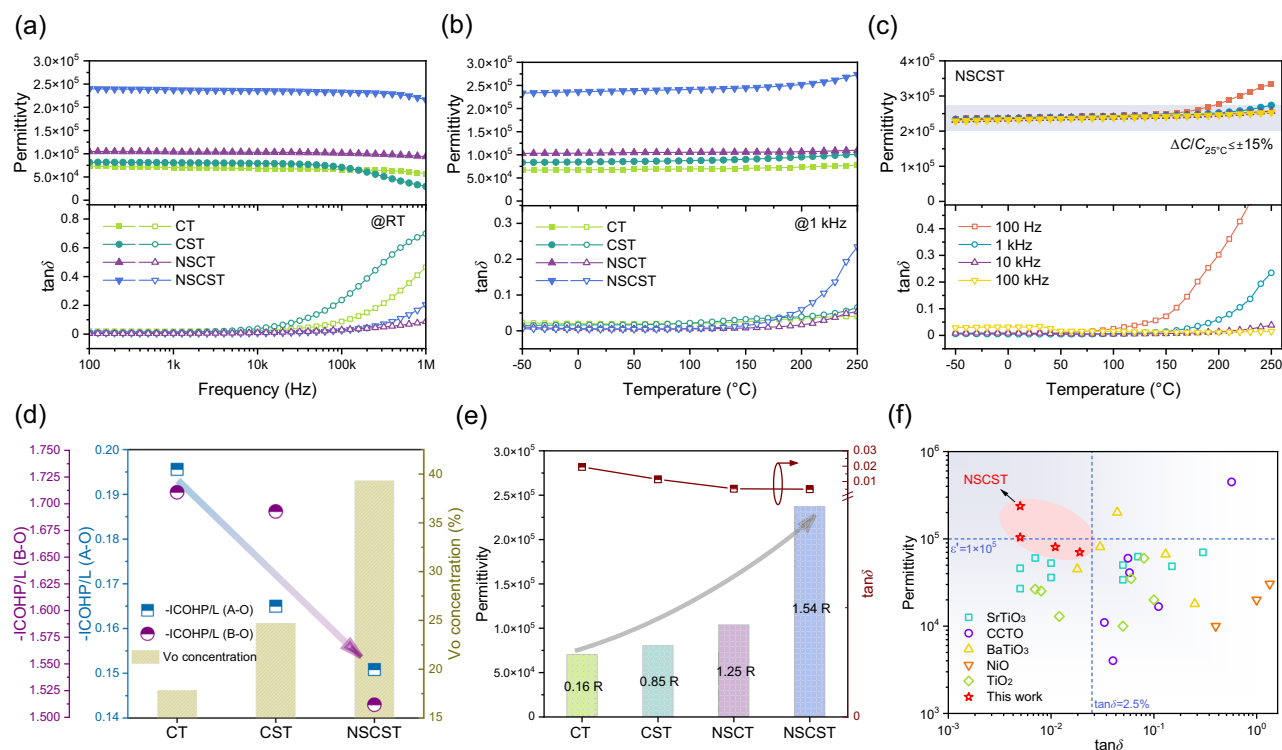


Fig. 4 | Dielectric responses of entropy-modulated CTO-based ceramics.

a Frequency-dependent permittivity and dielectric loss ($\tan\delta$) of CTO-based ceramics measured at room temperature (RT). **b** Temperature-dependent permittivity and dielectric loss ($\tan\delta$) of CTO-based ceramics measured at 1 kHz. **c** Temperature dependence of dielectric properties at various frequencies (100 Hz, 1 kHz, 10 kHz, 100 kHz) for the NSCST ceramic, indicating a small capacitance temperature

coefficient ($\Delta C/C_{25^\circ\text{C}}$) and an excellent thermal stability. **d** Variation in the chemical bonding property (ICOHP/L) and semiquantitative oxygen vacancy (V_o) concentration after entropy modulation. **e** Evolution of dielectric performance (RT, 1 kHz) as a function of configurational entropy. **f** Comparison between this work with other representative CP materials^{8,9,34,51–75}.

temperature stability were simultaneously achieved, outperforming other CP ceramic materials^{8,9,34,51–75} (Fig. 4f).

Our results prove that CP behavior can be achieved in CTO-based ceramics. By regulating the configurational entropy with proper substitutional elements and modulating chemical bonding properties, an increasing amount of lattice defects can be generated in CTO-based ceramics. The intentionally induced defects further interact to form defect dipoles and clusters, giving rise to dipole polarization while contributing to the localization of carriers, thus achieving an overall optimization of the dielectric performance. This strategy could be used in dielectric ceramics with similar structures to simultaneously obtain colossal permittivity and ultralow dielectric loss. This study offers an additional option for CP matrix determination and provides a feasible solution for the design of other defect-dependent functional materials.

Methods

Sample preparation

The CTO-based ceramics with the compositions of $\text{Ca}(\text{Ti}_{0.97}\text{Nb}_{0.015}\text{Er}_{0.015})\text{O}_3$, $(\text{Ca}_{0.5}\text{Sr}_{0.5})(\text{Ti}_{0.97}\text{Nb}_{0.015}\text{Er}_{0.015})\text{O}_3$, $(\text{Na}_{0.33}\text{Sm}_{0.33}\text{Ca}_{0.33})(\text{Ti}_{0.97}\text{Nb}_{0.015}\text{Er}_{0.015})\text{O}_3$, and $(\text{Na}_{0.25}\text{Sm}_{0.25}\text{Ca}_{0.25}\text{Sr}_{0.25})(\text{Ti}_{0.97}\text{Nb}_{0.015}\text{Er}_{0.015})\text{O}_3$ were fabricated by conventional solid-state reaction method. High-purity powders of CaCO_3 (99.5%, Aladdin, China), SrCO_3 (99.5%, Aladdin, China), Na_2CO_3 (99.99% Aladdin, China), Sm_2O_3 (99.9% Aladdin, China), TiO_2 (99% Aladdin, China), Nb_2O_5 (99.99% Aladdin, China), and Er_2O_3 (99.99% Aladdin, China) were used as raw materials and were weighed stoichiometrically (Na_2CO_3 5% excess). The powders were mixed thoroughly through ball-milling with ethanol for 24 h and were calcined in the air at 1100–1150 °C for 3 h before being ball-milled for the second time. The resulting powders were then mixed with 5 wt% PVA as a binder and pressed into pellets with a 12 mm diameter under axial pressure. The as-prepared cylindrical pellets were then heated at

600 °C for 3 h to eliminate the binder. Finally, the samples were sintered at 1400–1500 °C for 3 h in a 5% H_2/N_2 atmosphere. A group of pellets was sintered in air separately at corresponding temperatures for TSDC tests. Both sides of the samples were polished, coated with silver paste, and heated at 600 °C to obtain electrodes for electrical measurements.

Structure characterizations

X-ray diffraction (XRD, Bruker D8 Advance, Germany) with $\text{Cu K}\alpha$ X-ray source was used to identify the phase structure of the ceramic samples. To further confirm the structural parameters, Rietveld refinement was performed using the GSAS (General Structure Analysis System) software. The cross-sectional morphology of the microstructure and the elemental distribution were analyzed using scanning electron microscopy (SEM, Zeiss Merlin Compact, Germany), and the grain size distribution was calculated using the software “Nano Measurer”. The relative density of the samples was calculated according to the measured density and the theoretical density. X-ray photoelectron spectroscopy (XPS, Thermo Fisher Scientific ESCALAB 250Xi, the U. S.) was used to investigate the valence states of the elements and thus determine the possibly existing lattice defects. Thermogravimetry analysis (TGA, NETZSCH Scientific Instruments Trading Ltd X70, Germany) was used to visualize the oxygen refill process and quantify the bulk defect concentration. X-ray absorption near edge structure (XANES) of Ti K -edge was performed at BL14W1 beamlines at the Shanghai Synchrotron Radiation Facility (SSRF, Shanghai, China) in a transmission mode to evaluate the valence change. The absorption-edge position was defined as the photon energy of the peak in the first derivative spectrum. All test results were calibrated by aligning the absorption-edge energy shift of a Ti metal foil at 4966 eV. X-ray fluorescence (XRF, Thermo Fisher Scientific ARL PERFORM’X, the U.S.) analysis was conducted to provide quantitative elemental compositions of the synthesized ceramics.

Electrical and dielectric measurements

The dielectric properties were measured by a broadband dielectric/impedance spectrometer (Novocontrol Technologies GmbH & Co. KG, Germany), which was equipped with a liquid nitrogen cooling system to provide precise test results over a broad temperature and frequency range (−50 to 300 °C, 100 Hz–100 kHz). The thermally stimulated depolarization current (TSDC) measurements were performed using an electrometer/high resistance meter (B2985A, Keysight, the U. S.), equipped with the same quattro-temperature controller mentioned above. The pellets were first polarized under a DC electric field (E_p) at a certain temperature (T_p) for 10 min ($100 \text{ V/mm} \leq E_p \leq 200 \text{ V/mm}$; $T_p = 200^\circ\text{C}$), then rapidly cooled to -50°C to freeze the oriented defects, and gradually heated up to 300°C to gather the depolarization current. The complex impedance spectra (IS) were tested by an impedance/gain-phase analyzer (Solartron SI 1260) at various temperatures ($450\text{--}550^\circ\text{C}$) in the frequency range of 1 Hz to 1 MHz.

Calculations

The atomic size disorder. The atomic size disorder ($\Delta\delta_{\text{size}}^*$) of the ceramics can be calculated as follows:

$$\Delta\delta_{\text{size}}^* = \sqrt{\sum_{i=1}^n c_i \left(1 - \frac{r_i}{\sum_{i=1}^n c_i r_i}\right)^2} \quad (1)$$

where n , c_i , and r_i represent the number of elements, the atomic fraction of the i^{th} element, and the radii of the i^{th} element, respectively. In our case, the perovskite structure has A and B two cation sites, thus its $\Delta\delta_{\text{size}}^*$ can be modified as⁷⁶:

$$\Delta\delta_{\text{size}}^* = \sqrt{\Delta\delta_{\text{size(A)}}^2 + \Delta\delta_{\text{size(B)}}^2} \quad (2)$$

here, the ionic radii of the involved elements are 1.34 \AA (Ca^{2+}), 1.44 \AA (Sr^{2+}), 1.39 \AA (Na^+), 1.24 \AA (Sm^{3+}), 0.605 \AA (Ti^{4+}), 0.64 \AA (Nb^{5+}), and 0.89 \AA (Er^{3+})⁷⁷.

The distortion index. The parameter of distortion index (D) was applied to quantify the distortion extent within the octahedron, which is defined as^{78,79}:

$$D = \frac{1}{6} \sum_{i=1}^6 \frac{|l_i - l_{av}|}{l_{av}} \quad (3)$$

where l_i and l_{av} represent individual and average Ti–O bond lengths, respectively. The D values were calculated according to bond length data, which were obtained from Rietveld refinement results, as shown in Table S3.

DFT. All first-principles calculations were performed using the Vienna Ab Initio Simulation Package (VASP)^{80,81} based on density functional theory (DFT). The exchange-correlation function was performed using the generalized gradient approximation (GGA) of Perdew–Burke–Ernzerhof (PBE)⁸². Considering the strong correlation between localized Sm 4f and Ti 3d electrons, the DFT + U approximation was used for correction, with the effective U parameter taken to be 8 eV (Sm 4f), and 5.8 eV (Ti 3d)⁸³. The cut-off energy was set to 450 eV for the plane-wave based on the maximum energy of the atoms in the potential. The Brillouin zone of the reciprocal space was set to $1 \times 5 \times 3$. The force components for each atom were all less than 0.005 eV/\AA , and the total energy difference was less than 10^{-6} eV . All structures were fully relaxed before property calculations. The bonding information was obtained from the LOBSTER software⁸⁴, and the electron localization function was visualized by VESTA software⁸⁵.

Based on pristine CaTiO_3 (0R), a $5 \times 2 \times 2$ supercell (100 atoms) was used to obtain entropy-modified structures. The structures of CST

and NSCST were obtained by substituting 50% of Ca with Sr, and equally substituting 75% of Ca with Sr, Na, and Sm, respectively. Oxygen vacancies were obtained by removing 2 (3.33%), 4 (6.67%), and 6 (10%) O atoms from each entropy-modified structure. The bond strength was evaluated by the integrated crystal orbital Hamilton populations (ICOHP) value in a unit bond length (L). The integrated crystal orbital bond index (ICOBI) of A–O and B–O bonds, the band structure, and the corresponding density of states (DOS) were acquired for CT (0Vo), CST (2Vo), and NSCST (4Vo) systems.

Data availability

The authors declare that the data supporting the findings of this study are available within the paper and its Supplementary Information files. The source data used in this study have been deposited in the Figshare database under accession code <https://doi.org/10.6084/m9.figshare.28280039>.

References

- Yang, B. B. et al. Engineering relaxors by entropy for high energy storage performance. *Nat. Energy* **8**, 956–964 (2023).
- Wang, G. et al. Electroceramics for high-energy density capacitors: current status and future perspectives. *Chem. Rev.* **121**, 6124–6172 (2021).
- Buscaglia, M. T. et al. High dielectric constant and frozen macroscopic polarization in dense nanocrystalline BaTiO_3 ceramics. *Phys. Rev. B* **73**, 064114 (2006).
- Subramanian, M. A., Li, D., Duan, N., Reisner, B. A. & Sleight, A. W. High dielectric constant in $\text{ACu}_3\text{Ti}_4\text{O}_{12}$ and $\text{ACu}_3\text{Ti}_3\text{FeO}_{12}$ phases. *J. Solid State Chem.* **151**, 323–325 (2000).
- Kozuka, Y. et al. Two-dimensional normal-state quantum oscillations in a superconducting heterostructure. *Nature* **462**, 487–490 (2009).
- Sinclair, D. C., Adams, T. B., Morrison, F. D. & West, A. R. $\text{CaCu}_3\text{Ti}_4\text{O}_{12}$: One-step internal barrier layer capacitor. *Appl. Phys. Lett.* **80**, 2153–2155 (2002).
- Lunkenheimer, P., Fichtl, R., Ebbinghaus, S. G. & Loidl, A. Non-intrinsic origin of the colossal dielectric constants in $\text{CaCu}_3\text{Ti}_4\text{O}_{12}$. *Phys. Rev. B* **70**, 172102 (2004).
- Hu, W. B. et al. Electron-pinned defect-dipoles for high-performance colossal permittivity materials. *Nat. Mater.* **12**, 821–826 (2013).
- Tan, J. L., Guo, Y., Ren, F. T. & Zhao, J. C. Giant dielectric response and grain heterogeneity of $\text{Y}_{2/3}\text{Cu}_3\text{Ti}_4\text{O}_{12}\text{--TiO}_2$ composite ceramics fabricated by hydrothermal process. *J. Am. Ceram. Soc.* **106**, 3462–3470 (2023).
- Wang, B. et al. Ultralow dielectric loss in Y-doped SrTiO_3 colossal permittivity ceramics via designing defect chemistry. *J. Am. Ceram. Soc.* **103**, 6811–6821 (2020).
- Tang, L. N. et al. High configuration entropy activated lattice oxygen for O_2 formation on perovskite electrocatalyst. *Adv. Funct. Mater.* **32**, 2112157 (2022).
- Shi, Y. C. et al. Role of mixed entropy in sintering of manganite-based perovskite oxides: Faster densification with delayed grain growth. *Acta Mater.* **271**, 119906 (2024).
- Park, J. et al. Accurate prediction of oxygen vacancy concentration with disordered A-site cations in high-entropy perovskite oxides. *Npj Comput. Mater.* **9**, 29 (2023).
- Zhang, Y. et al. Stabilizing oxygen vacancy in entropy-engineered CoFe_2O_4 -type catalysts for Co-prosperity of efficiency and stability in an oxygen evolution reaction. *ACS Appl. Mater. Inter.* **12**, 32548–32555 (2020).
- Sarkar, A. et al. High-entropy oxides: fundamental aspects and electrochemical properties. *Adv. Mater.* **31**, 1806236 (2019).
- Qin, S., Becerro, A. I., Seifert, F., Gottsmann, J. & Jiang, J. Z. Phase transitions in $\text{Ca}_{1-x}\text{Sr}_x\text{TiO}_3$ perovskites: effects of composition and temperature. *J. Mater. Chem.* **10**, 1609–1615 (2000).

17. Mishra, S. K. et al. A combined X-ray diffraction and Raman scattering study of the phase transitions in $\text{Sr}_{1-x}\text{Ca}_x\text{TiO}_3$ ($x=0.04, 0.06$, and 0.12). *J. Solid State Chem.* **178**, 2846–2857 (2005).
18. Li, J. Y., Li, S. T. & Alim, M. A. The effect of reducing atmosphere on the SrTiO_3 based varistor-capacitor materials. *J. Mater. Sci. Mater. Electron.* **17**, 503–508 (2006).
19. Zhou, L., Liu, J. X., Tu, T. Z., Wu, Y. & Zhang, G. J. Fast grain growth phenomenon in high-entropy ceramics: a case study in rare-earth hexaaluminates. *J. Adv. Ceram.* **12**, 111–121 (2023).
20. Irvine, J. T. S., Sinclair, D. C. & West, A. R. Electroceramics: characterization by impedance spectroscopy. *Adv. Mater.* **2**, 132–138 (1990).
21. Zhang, L. & Tang, Z.-J. Polaron relaxation and variable-range-hopping conductivity in the giant-dielectric-constant material $\text{CaCu}_3\text{Ti}_4\text{O}_{12}$. *Phys. Rev. B* **70**, 174306 (2004).
22. He, Z. C. et al. Origin of low dielectric loss and giant dielectric response in (Nb+Al) co-doped strontium titanate. *J. Am. Ceram. Soc.* **101**, 5089–5097 (2018).
23. Zhang, X. et al. Simultaneously achieving colossal permittivity, ultralow dielectric loss tangent, and high insulation resistivity in Er-doped SrTiO_3 ceramics via oxygen vacancy regulation. *ACS Appl. Mater. Inter.* **14**, 48821–48832 (2022).
24. Liu, W. & Randall, C. A. Thermally stimulated relaxation in Fe-doped SrTiO_3 systems: I. Single crystals. *J. Am. Ceram. Soc.* **91**, 3245–3250 (2008).
25. Zhang, J., Yue, Z., Luo, Y., Zhang, X. & Li, L. Understanding the thermally stimulated relaxation and defect behavior of Ti-containing microwave dielectrics: a case study of BaTi_4O_9 . *Mater. Des.* **130**, 479–487 (2017).
26. Guo, W., Zhang, J., Luo, Y., Yue, Z. & Li, L. Microwave dielectric properties and thermally stimulated depolarization of Al-doped $\text{Ba}_4(\text{Sm}, \text{Nd})_{9.33}\text{Ti}_{18}\text{O}_{54}$ ceramics. *J. Am. Ceram. Soc.* **102**, 5494–5502 (2019).
27. Song, H. et al. Review of the thermally stimulated depolarization current (TSDC) technique for characterizing dielectric materials. *J. Korean Ceram. Soc.* **60**, 747–759 (2023).
28. Karasawa, J., Takaku, H. & Fukami, T. Localized polarization in strontium titanate crystal. *Jpn. J. Appl. Phys.* **35**, 5129–5131 (1996).
29. Hino, T. Thermally stimulated characteristics in solid dielectrics. *IEEE Trans. Electr. Insul.* **15**, 301–311 (1980).
30. Lee, S. J., Kang, K. Y. & Han, S. K. Low-frequency dielectric relaxation of BaTiO_3 thin-film capacitors. *Appl. Phys. Lett.* **75**, 1784–1786 (1999).
31. Yoon, S. H., Randall, C. A. & Hur, K. H. Correlation between resistance degradation and thermally stimulated depolarization current in acceptor (Mg)-doped BaTiO_3 submicrometer fine-grain ceramics. *J. Am. Ceram. Soc.* **93**, 1950–1956 (2010).
32. Zhang, X. H. et al. Microwave dielectric properties and thermally stimulated depolarization currents study of $(1-x)\text{Ba}_{0.6}\text{Sr}_{0.4}\text{La}_4\text{Ti}_4\text{O}_{15-x}\text{TiO}_2$ ceramics. *J. Am. Ceram. Soc.* **97**, 3170–3176 (2014).
33. Fan, J. T., Yang, T. T., Cao, Y. F. & Liang, J. Y. Ultralow dielectric loss in Tb plus Ta-modified TiO_2 giant dielectric ceramics via designing defect chemistry. *J. Am. Ceram. Soc.* **106**, 1859–1869 (2023).
34. He, Z. C. et al. Abnormal dielectric relaxations and giant permittivity in SrTiO_3 ceramic prepared by plasma activated sintering. *J. Am. Ceram. Soc.* **105**, 4143–4151 (2022).
35. Li, J. et al. Microstructure and dielectric properties of (Nb+In) co-doped rutile TiO_2 ceramics. *J. Appl. Phys.* **116**, 074105 (2014).
36. Li, J. Y., Zhao, X. T., Gu, F. & Li, S. T. Defects and dc electrical degradation in $\text{CaCu}_3\text{Ti}_4\text{O}_{12}$ ceramics: role of oxygen vacancy migration. *Appl. Phys. Lett.* **100**, 202905 (2012).
37. Wang, C. C. & Zhang, L. W. Surface-layer effect in $\text{CaCu}_3\text{Ti}_4\text{O}_{12}$. *Appl. Phys. Lett.* **88**, 042906 (2006).
38. Ang, C., Yu, Z. & Cross, L. E. Oxygen-vacancy-related low-frequency dielectric relaxation and electrical conduction in Bi: SrTiO_3 . *Phys. Rev. B* **62**, 228–236 (2000).
39. Huang, Y. C., Li, K. S., Li, S. Q., Lin, Y., Liu, H. & Tong, Y. X. Ultrathin Bi_2MoO_6 nanosheets for photocatalysis: performance enhancement by atomic interfacial engineering. *Chem. Sel.* **3**, 7423–7428 (2018).
40. Hou, L. L., Zhang, M., Guan, Z. J., Li, Q. Y. & Yang, J. J. Effect of annealing ambience on the formation of surface/bulk oxygen vacancies in TiO_2 for photocatalytic hydrogen evolution. *Appl. Surf. Sci.* **428**, 640–647 (2018).
41. Ramos-Moore, E., Ferrari, P., Diaz-Droguett, D. E., Lederman, D. & Evans, J. T. Raman and x-ray photoelectron spectroscopy study of ferroelectric switching in $\text{Pb}(\text{Nb}, \text{Zr}, \text{Ti})\text{O}_3$ thin films. *J. Appl. Phys.* **111**, 014108 (2012).
42. Ehre, D., Cohen, H., Lyahovitskaya, V. & Lubomirsky, I. X-ray photoelectron spectroscopy of amorphous and quasiamorphous phases of BaTiO_3 and SrTiO_3 . *Phys. Rev. B* **77**, 184106 (2008).
43. Becke, A. D. & Edgecombe, K. E. A simple measure of electron localization in atomic and molecular-systems. *J. Chem. Phys.* **92**, 5397–5403 (1990).
44. Shi, M. et al. Effects of oxygen vacancy on bond ionicity, lattice energy, and microwave dielectric properties of CeO_2 ceramics with Yb^{3+} substitution. *J. Adv. Ceram.* **13**, 247–254 (2024).
45. Wexler, R. B., Gautam, G. S., Stechel, E. B. & Carter, E. A. Factors governing oxygen vacancy formation in oxide perovskites. *J. Am. Chem. Soc.* **143**, 13212–13227 (2021).
46. Tuichai, W. et al. Origin(s) of the apparent colossal permittivity in $(\text{In}_{1/2}\text{Nb}_{1/2})_x\text{Ti}_{1-x}\text{O}_2$: clarification on the strongly induced Maxwell-Wagner polarization relaxation by DC bias. *RSC Adv.* **7**, 95–105 (2017).
47. Wang, L. et al. Effect of rare-earth (RE) ionic radius on the dielectric properties of $\text{Sr}_{99\%}\text{RE}_{1\%}\text{TiO}_3$ (RE = La, Nd, Yb) single crystals. *Crys-tEngComm* **25**, 95–107 (2022).
48. Fan, J. T. et al. Giant dielectric response and relaxation behavior in (Tm+Ta) co-doped TiO_2 ceramics. *Phys. Chem. Chem. Phys.* **24**, 4759–4768 (2022).
49. Han, Y. et al. Ultra-dense dislocations stabilized in high entropy oxide ceramics. *Nat. Commun.* **13**, 2871 (2022).
50. Pan, W. G. et al. Defect engineering toward the structures and dielectric behaviors of (Nb, Zn) co-doped SrTiO_3 ceramics. *J. Eur. Ceram. Soc.* **40**, 49–55 (2020).
51. Boonlakhorn, J., Kidkhunthod, P., Chanlek, N. & Thongbai, P. (Al^{3+} , Nb^{5+}) co-doped $\text{CaCu}_3\text{Ti}_3\text{O}_{12}$: an extended approach for acceptor-donor heteroatomic substitutions to achieve high-performance giant-dielectric permittivity. *J. Eur. Ceram. Soc.* **38**, 137–143 (2018).
52. Cai, J. H., Qi, J. L., Yang, Y. Y., Zhang, X. Y. & Lin, Y. H. Colossal permittivity and ultralow dielectric loss in Nb-doped SrTiO_3 ceramics. *J. Adv. Ceram.* **12**, 2247–2256 (2023).
53. Dong, W. et al. Colossal dielectric behavior of Ga+Nb co-doped rutile TiO_2 . *ACS Appl. Mater. Inter.* **7**, 25321–25325 (2015).
54. Fan, J., Chen, Y., Long, Z., He, G. & Hu, Z. Grain-boundary engineering inducing thermal stability, low dielectric loss and high energy storage in Ta+Ho co-doped TiO_2 ceramics. *Ceram. Int.* **48**, 21543–21551 (2022).
55. Fan, J. et al. Thermal stable and ultralow dielectric loss in $(\text{Gd}_{0.5}\text{Ta}_{0.5})_x\text{Ti}_{1-x}\text{O}_2$ giant permittivity ceramics by defect engineering. *J. Materiomics* **9**, 157–165 (2023).
56. Fan, J., He, G., Long, Z. & Hu, Z. High insulation resistivity and low dielectric loss in (Ta, Al)-codoped BaTiO_3 colossal permittivity materials. *J. Am. Ceram. Soc.* **107**, 4854–4863 (2024).
57. Fan, J. T. et al. Colossal permittivity of Sb and Ga co-doped rutile TiO_2 ceramics. *Ceram. Int.* **45**, 1001–1010 (2019).
58. Fan, J. T., Yang, T. T., Cao, Y. F. & Liang, J. Y. Ultralow dielectric loss in Tb+Ta-modified TiO_2 giant dielectric ceramics via designing defect chemistry. *J. Am. Ceram. Soc.* **106**, 1859–1869 (2023).
59. Hu, W. B. et al. Colossal dielectric permittivity in (Nb+Al) codoped rutile TiO_2 ceramics: Compositional gradient and local structure. *Chem. Mater.* **27**, 4934–4942 (2015).

60. Li, L. X., Xie, J. L., Wang, M. L. & Zhang, K. Colossal permittivity (Nb, Mg) co-doped BaTiO₃ ceramics with excellent temperature stability and high insulation resistivity. *Ceram. Int.* **47**, 10072–10078 (2021).
61. Li, Y. H., Fang, L., Liu, L. J., Huang, Y. M. & Hu, C. Z. Giant dielectric response and charge compensation of Li- and Co-doped NiO ceramics. *Mater. Sci. Eng. B-Adv.* **177**, 673–677 (2012).
62. Liang, P. F., Yang, Z. P., Chao, X. L. & Liu, Z. H. Giant dielectric constant and good temperature stability in Y_{2/3}Cu₃Ti₄O₁₂ ceramics. *J. Am. Ceram. Soc.* **95**, 2218–2225 (2012).
63. Luo, B. C. et al. Giant permittivity and low dielectric loss of Fe doped BaTiO₃ ceramics: Experimental and first-principles calculations. *J. Eur. Ceram. Soc.* **38**, 1562–1568 (2018).
64. Peng, Z. H. et al. Fabrication and characterization of CdCu₃Ti₄O₁₂ ceramics with colossal permittivity and low dielectric loss. *Mater. Lett.* **210**, 301–304 (2018).
65. Pongha, S., Thongbai, P., Yamwong, T. & Maensiri, S. Giant dielectric response and polarization relaxation mechanism in (Li,V)-doped NiO ceramics. *Scr. Mater.* **60**, 870–873 (2009).
66. Qin, M. J. et al. Point defect structure of La-doped SrTiO₃ ceramics with colossal permittivity. *Acta Mater.* **164**, 76–89 (2019).
67. Ren, L. L., Yang, L. J., Xu, C., Zhao, X. T. & Liao, R. J. Improvement of breakdown field and dielectric properties of CaCu₃Ti₄O₁₂ ceramics by Bi and Al co-doping. *J. Alloy. Compd.* **768**, 652–658 (2018).
68. Ren, P. R., He, J. J., Wang, X., Sun, M. Q., Zhang, H. & Zhao, G. Y. Colossal permittivity in niobium doped BaTiO₃ ceramics annealed in N₂. *Scr. Mater.* **146**, 110–114 (2018).
69. Tkach, A., Okhay, O., Almeida, A. & Vilarinho, P. M. Giant dielectric permittivity and high tunability in Y-doped SrTiO₃ ceramics tailored by sintering atmosphere. *Acta Mater.* **130**, 249–260 (2017).
70. Tsuji, K. et al. Valence and electronic trap states of manganese in SrTiO₃-based colossal permittivity barrier layer capacitors. *RSC Adv.* **6**, 92127–92133 (2016).
71. Wang, Z. J. et al. Dielectric relaxation in Zr-doped SrTiO₃ ceramics sintered in N₂ with giant permittivity and low dielectric loss. *J. Am. Ceram. Soc.* **98**, 476–482 (2015).
72. Wu, J. B., Nan, C. W., Lin, Y. H. & Deng, Y. Giant dielectric permittivity observed in Li and Ti doped NiO. *Phys. Rev. Lett.* **89**, 217601 (2002).
73. Wu, R. F. et al. High thermal sensitivity and dielectric constants in CaCu₃Ti₄O₁₂-LaMn_{1-x}Fe_xO₃ composite ceramics by designing sandwich and core-shell structure. *J. Eur. Ceram. Soc.* **45**, 117041 (2025).
74. Xue, K. & Li, L. Colossal permittivity in Ta-doped SrTiO₃ ceramics induced by interface effects and defect structure: An experimental and theoretical study. *Ceram. Int.* **49**, 20388–20397 (2023).
75. Zhao, F. et al. Dielectric abnormalities in BaTiO₃(Ni_{1/2}W_{1/2})O₃ giant dielectric constant ceramics. *Appl. Phys. Lett.* **91**, 052903 (2007).
76. Wright, A. J. et al. Size disorder as a descriptor for predicting reduced thermal conductivity in medium- and high-entropy pyrochlore oxides. *Scr. Mater.* **181**, 76–81 (2020).
77. Shannon, R. D. Revised effective ionic radii and systematic studies of interatomic distances in halides and chalcogenides. *Acta Crystallogr. A* **32**, 751–767 (1976).
78. Kim, D. B., Jo, K. S., Park, S. J. & Cho, Y. S. Contribution of anisotropic lattice-strain to piezoelectricity and electromechanical power generation of flexible inorganic halide thin films. *Adv. Energy Mater.* **12**, 2103329 (2022).
79. Robinson, K., Gibbs, G. V. & Ribbe, P. H. Quadratic elongation: a quantitative measure of distortion in coordination polyhedra. *Science* **172**, 567–570 (1971).
80. Kresse, G. & Furthmüller, J. Efficiency of ab-initio total energy calculations for metals and semiconductors using a plane-wave basis set. *Comp. Mater. Sci.* **6**, 15–50 (1996).
81. Kresse, G. & Furthmüller, J. Efficient iterative schemes for ab initio total-energy calculations using a plane-wave basis set. *Phys. Rev. B* **54**, 11169–11186 (1996).
82. Perdew, J. P., Burke, K. & Ernzerhof, M. Generalized gradient approximation made simple. *Phys. Rev. Lett.* **77**, 3865–3868 (1996).
83. Anisimov, V. I., Zaanen, J. & Andersen, O. K. Band theory and Mott insulators: Hubbard U instead of Stoner I. *Phys. Rev. B* **44**, 943–954 (1991).
84. Dronskowski, R. & Blochl, P. E. Crystal orbital Hamilton populations (COHP): energy-resolved visualization of chemical bonding in solids based on density-functional calculations. *J. Phys. Chem.* **97**, 8617–8624 (1993).
85. Momma, K. & Izumi, F. VESTA 3 for three-dimensional visualization of crystal, volumetric and morphology data. *J. Appl. Crystallogr.* **44**, 1272–1276 (2011).

Acknowledgements

This work was financially supported by the National Key Research Program of China (grant No. 2021YFB3800601) and the Basic Science Center Project of the National Natural Science Foundation of China (NSFC) under grant No. 52388201 (Y.-H.L.).

Author contributions

Y.-H. Lin and J. Cai conceived the study. J. Cai wrote the manuscript, conducted the experiments, and analyzed the data in this study. B. Wei carried out the DFT calculations. S. Lan, J. Qi and C.-W. Nan assisted in the writing of the manuscript. All authors discussed and revised the manuscript.

Competing interests

The authors declare no competing interests.

Additional information

Supplementary information The online version contains supplementary material available at <https://doi.org/10.1038/s41467-025-59226-y>.

Correspondence and requests for materials should be addressed to Yuan-Hua Lin.

Peer review information *Nature Communications* thanks Hangfeng Zhang and the other anonymous reviewer(s) for their contribution to the peer review of this work. A peer review file is available.

Reprints and permissions information is available at <http://www.nature.com/reprints>

Publisher's note Springer Nature remains neutral with regard to jurisdictional claims in published maps and institutional affiliations.

Open Access This article is licensed under a Creative Commons Attribution-NonCommercial-NoDerivatives 4.0 International License, which permits any non-commercial use, sharing, distribution and reproduction in any medium or format, as long as you give appropriate credit to the original author(s) and the source, provide a link to the Creative Commons licence, and indicate if you modified the licensed material. You do not have permission under this licence to share adapted material derived from this article or parts of it. The images or other third party material in this article are included in the article's Creative Commons licence, unless indicated otherwise in a credit line to the material. If material is not included in the article's Creative Commons licence and your intended use is not permitted by statutory regulation or exceeds the permitted use, you will need to obtain permission directly from the copyright holder. To view a copy of this licence, visit <http://creativecommons.org/licenses/by-nc-nd/4.0/>.

© The Author(s) 2025